High Power Laser Science and Engineering, (2022), Vol. 10, e39, 8 pages.
doi:10.1017/hpl.2022.30

HIGH POWER LASER SCIENCE AND ENGINEERING

RESEARCH ARTICLE

Effects of second-order dispersion of ultrashort laser pulse on stimulated Raman scattering

Yanqing Deng[1,2], Dongning Yue[1,2], Mufei Luo[1,2], Xu Zhao[1,2], Yaojun Li[1,2], Xulei Ge[1,2], Feng Liu[1,2], Suming Weng[1,2], Min Chen[1,2], Xiaohui Yuan[1,2], and Jie Zhang[1,2]

[1] *Key Laboratory for Laser Plasmas (Ministry of Education), School of Physics and Astronomy, Shanghai Jiao Tong University, Shanghai, China*

[2] *Collaborative Innovation Center of IFSA, Shanghai Jiao Tong University, Shanghai, China*

(Received 29 July 2022; revised 26 September 2022; accepted 26 October 2022)

Abstract

The influence of second-order dispersion (SOD) on stimulated Raman scattering (SRS) in the interaction of an ultrashort intense laser with plasma was investigated. More significant backward SRS was observed with the increase of the absolute value of SOD ($|\psi_2|$). The integrated intensity of the scattered light is positively correlated to the driver laser pulse duration. Accompanied by the side SRS, filaments with different angles along the laser propagation direction were observed in the transverse shadowgraph. A model incorporating Landau damping and above-threshold ionization was developed to explain the SOD-dependent angular distribution of the filaments.

Keywords: second-order dispersion; stimulated Raman scattering; ultrashort intense laser

1. Introduction

Stimulated Raman scattering (SRS) is an important parametric instability in laser propagation in underdense plasma[1]. It is a three-wave process with a pump electromagnetic (EM) wave (ω_0, $\mathbf{k}_0$) decaying into a scattered EM wave (ω_1, $\mathbf{k}_1$) and an electron plasma wave (ω_{epw}, $\mathbf{k}_{epw}$). The instability arises in the region where the plasma density is equal to or less than a quarter of critical density $n_c = m_e\omega_0^2/\left(4\pi e^2\right)$, with m_e being the electron mass and e the electron charge. Due to issues of reduced laser absorption and detrimental hot-electron generation, SRS has been extensively investigated in inertial confinement fusion studies, where multiple-beam high-energy nanosecond laser pulses are usually adopted[2].

In addition to long laser pulses, SRS also plays key roles in ultrashort relativistic-intensity laser–plasma interactions ($> 10^{18}$ W/cm^2)[3–8]. It continuously scatters the laser energy and weakens its stable propagation, impacting on various applications, including laser wakefield acceleration (LWFA)[9], novel-mechanism ion acceleration[10–12] and high-brightness X-ray generation[13,14]. Besides the drawbacks, SRS may also benefit some applications. It can enhance the electron injection in LWFA[15], and serve as a diagnostic of electron density[16,17], laser intensity[8,17,18] and plasma temperature[19].

In past studies, the chirp of ultrashort laser pulses has been proposed to control the SRS process. It can be adjusted by introducing second-order dispersion (SOD) (ψ_2), which is also known as the group velocity dispersion, into the laser pulse[20–25]. Theoretical research shows that a positive chirp can enhance SRS and create a large-amplitude plasma wave. A negative chirp, on the other hand, may suppress SRS[26–29]. However, only a limited number of experiments have been conducted, and inconsistent conclusions were drawn[21,22]. The dependence of Raman scattering on the SOD of ultrashort laser pulses remains elusive, and the role of subsequently varied pulse duration is still unclear.

In this paper, the influence of SOD on SRS is experimentally studied. Optical spectroscopy and shadowgraphy were used to measure backward stimulated Raman scattering (B-SRS), side stimulated Raman scattering (S-SRS) and forward stimulated Raman scattering (F-SRS), respectively.

Correspondence to: M. Chen and X. Yuan, Key Laboratory for Laser Plasmas (Ministry of Education), School of Physics and Astronomy, Shanghai Jiao Tong University, Shanghai 200240, China. Email: minchen@sjtu.edu.cn (M. Chen); xiaohui.yuan@sjtu.edu.cn (X. Yuan)

For both positive and negative ψ_2, it was observed that the integrated B-SRS signal grows with the pulse duration. Side scattering-induced filaments were observed to be more obvious with increasing $|\psi_2|$. The angles of these filaments are spatially dependent and sensitive to ψ_2, which is explained by an analytical model. Moreover, a suppression on F-SRS was observed with a negative ψ_2.

2. Experimental setup

The experiment was performed with the 200 TW Ti:sapphire laser system at Shanghai Jiao Tong University[30]. The schematic setup is shown in Figure 1(a). The main laser beam was focused by an F/4 off-axis parabola (OAP) mirror to a spot of 6 μm in diameter, containing approximately 25% of the laser energy. The laser has a central wavelength of $\lambda_0 = 800$ nm with a bandwidth of 70 nm at full width at half maximum (FWHM). The pulse duration, τ_L, is adjusted by introducing ψ_2 through an acousto-optic programmable dispersive filter, namely Dazzler[31]. In general, the temporal profile of a Gaussian pulse is given by the following:

$$a(t) = a_0 \exp\left(-\frac{t^2}{\tau^2}\right) \exp\left[i\omega_0 t\,(1+\beta t)\right], \quad (1)$$

$$\tau = \left[\left(4+\Delta\omega^4\psi_2^2\right)/\Delta\omega^2\right]^{1/2}, \quad (2)$$

$$\beta = \Delta\omega^4\psi_2/\left[2\omega_0\left(4+\Delta\omega^4\psi_2^2\right)\right], \quad (3)$$

where a_0 is the normalized amplitude, $\Delta\omega$ is half of the frequency bandwidth, and τ and β represent the ψ_2-dependent laser duration and chirp, respectively. Here higher-order dispersion is not considered. From Equation (2), one can see that the pulse can be symmetrically stretched by adding negative or positive ψ_2. The instant frequency $\omega(t)$ changes linearly in time with the chirp rate $2\omega_0\beta$. In our experiment, ψ_2 was adjusted from –3000 to +3000 fs^2. Here, $\psi_2 = 0$ represents no SOD and it corresponds to a transform-limited pulse with a duration of 29 fs. The positive (negative) ψ_2 denotes a positively (negatively) chirped laser pulse. The main pulse parameters at different ψ_2 are summarized in Table 1. The laser was focused on a helium gas jet target at 275 μm before the nozzle center and 1400 μm above the exit.

A probe pulse was split from the main pulse and frequency doubled. The timing between the probe and the main pulse was adjusted by a variable delay line as shown in Figure 1(a). After passing through the interaction region, the probe beam was further split by a biprism for interferometric and shadowgraphic measurements. Figure 1(b) shows the typical density distribution of a plasma channel from the Abel-inverted interferogram, where $z = 0$ μm represents the laser axis and $x = 0$ μm denotes the nozzle center. It shows that the plasma density along the laser axis comprises a long density up-ramp and a plateau of approximately 1×10^{20} cm^{-3}. Figure 1(c) displays the typical plasma

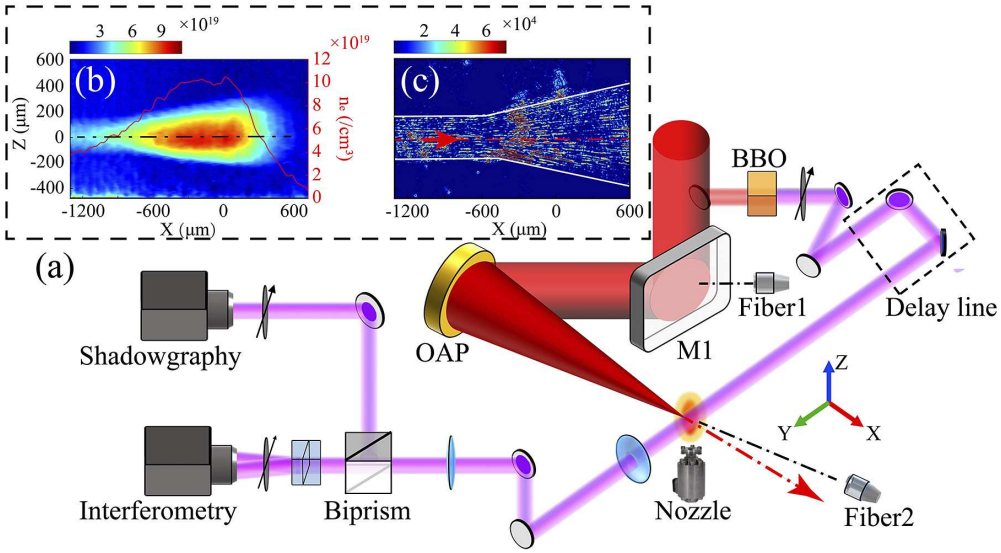

Figure 1. (a) Schematic layout of the experimental setup. (b) Image of the typical electron density distribution and the on-axis density lineout (red solid line) with $\psi_2 = 0$. (c) The corresponding shadowgraph, where the color bar denotes the signal count in the charge-coupled device (CCD). The laser is incident from the left-hand side. Here, $t = 0$ ps is denoted when the main laser is at $x = -1300$ μm. The interferogram and shadowgraphs were taken at $t = 7.0$ ps.

Table 1. Laser parameters for different ψ_2 with fixed energy (2.2 J).

$\lvert\psi_2\rvert$ (fs^2)	0	500	1000	2000	3000
τ_L (fs)	29.0	93.0	188.4	361.6	550.0
β ($\times 10^{-5}$)	0	17.01	8.32	4.51	2.92
a_0	5.60	3.12	2.20	1.58	1.28

https://doi.org/10.1017/hpl.2022.30 Published online by Cambridge University Press

channel in the shadowgraph with $\psi_2 = 0$. Two fiber-optic spectrometers with fiber-coupled lenses were installed to measure the optical spectra of back-scattered (Fiber 1 in Figure 1(a)) and transmitted light (Fiber 2 in Figure 1(a)). The detection ranges are 500–1200 and 200–1100 nm, respectively.

3. Experimental results and analysis

3.1. Influence of ψ_2 on B-SRS

Figure 2 shows spectra of the back-scattered light under different ψ_2. It shows that the larger $|\psi_2|$ is, the stronger the back-scattering is. For both negative and positive ψ_2, the back-scattering spectra are almost identical for the same $|\psi_2|$. When $|\psi_2| \geqslant 1000$ fs^2, clear Stokes sidebands with a regular interval were observed, indicating a substantial stronger excitation of B-SRS[32]. From the match condition, $\omega_0 = \omega_1 \pm \omega_{pe}$ (ω_{pe} is the plasma frequency), we deduce that B-SRS occurs in the density region $n_e \approx 5 \times 10^{18}$ cm^{-3}.

To quantitatively compare the results, the red-shifted back-scattering (840–1100 nm) was integrated and plotted as a function of pulse duration τ_L (shown in Figure 3). The integrated B-SRS signal has an exponential-like distribution for both negative and positive chirps. Although from Equation (2), the laser pulses with the same $|\psi_2|$ have the same pulse duration, the integrated signal is dependent on the sign of laser chirp. A larger signal was acquired with a positive chirp.

In order to understand the influence of ψ_2 on B-SRS, a simple model is used. For an ultrashort laser propagating in a homogeneous plasma, the growth rate of SRS is given by the following[3]:

$$\gamma_0 \approx \frac{k_{epw}}{8} v_{osc} \left[\frac{\omega_{pe}^2}{\omega_{epw}\left(\omega_0 - \omega_{epw}\right)} \right]^{1/2}, \tag{4}$$

where v_{osc} is the electron oscillation velocity.

The analysis of the Stokes sidebands has shown that B-SRS arises in the region of non-relativistic laser intensity ($I_0 \leqslant 1.0 \times 10^{18}$ W/cm^2 for $\psi_2 = 0$) far before the focus. Thus, the electron oscillation velocity is estimated using $v_{osc} = a_0 c$, where c is the speed of light. To evaluate γ_0, plasma temperature T_e is required to infer the thermal velocity $v_{th} = \sqrt{T_e/m_e}$, which is further used to estimate the electron-plasma-wave frequency from the dispersion relation, $\omega_{epw}^2 = \omega_{pe}^2 + 3k_{epw}^2 v_{th}^2$. The quasi-static model of above-threshold ionization (ATI) is applicable to get the plasma temperature[33,34]. In the model, the phase mismatch, $\Delta\phi$, between the electron releasing position and the crest of pump light, produces electrons with residual kinetic energy $\varepsilon = 2E_q \sin^2 \Delta\phi$, where E_q is the electron ponderomotive potential. Over a laser cycle, the averaged ATI energy is given by the following[34]:

$$\langle \varepsilon \rangle = \frac{\int_0^{\frac{\pi}{2}} 2E_q W(t) \cos\phi^2 \mathrm{d}\phi}{\int_0^{\frac{\pi}{2}} W(t) \mathrm{d}\phi}, \tag{5}$$

where $W(t)$ is the tunneling ionization rate, which is dependent on the strength of the electric field E_l and the ionization potential E_i of the target ion[35]. Then, T_e could be calculated by $T_e \sim \frac{2}{3Z} \sum \langle \varepsilon_i \rangle$. For a helium target, E_i is 13.6 and 54.4 eV to generate He^+ and He^{2+}, respectively. However, we ignore the contribution of He^+ to T_e since He^+ could be generated by the amplified spontaneous emission instead of the main pulse.

As SRS develops in the rising edge of the laser pulse, where different wavelength components are contained, the chirp effect is straightforward. To simplify the estimation and investigate the effect of the laser wavelength on SRS growth, two cases with different single wavelengths, simulating the positive and negative chirps, were used to calculate the growth rates. We take $\lambda_0 = 835$ and 765 nm, corresponding to our laser bandwidth, for cases of positive and negative ψ_2, respectively.

The inset in Figure 3 shows the growth rate as a function of pulse duration. Here, γ_0 decreases with τ_L and follows the scale of $\sim 1/\sqrt{\tau_L}$. It is 8.2% higher for long-wavelength

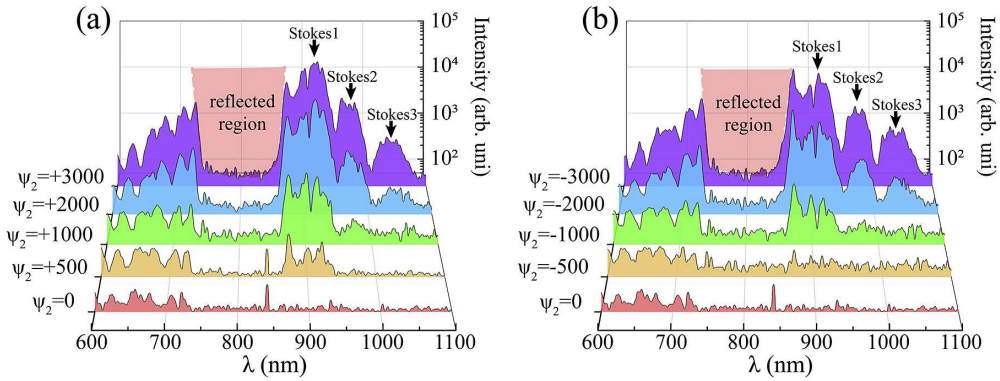

Figure 2. The back-scattered light spectra with various (a) positive and (b) negative second-order dispersions. The absence of light within 730–870 nm is due to the total reflection of the M1 mirror in front of the collection fiber (Fiber 1 in Figure 1(a)).

https://doi.org/10.1017/hpl.2022.30 Published online by Cambridge University Press

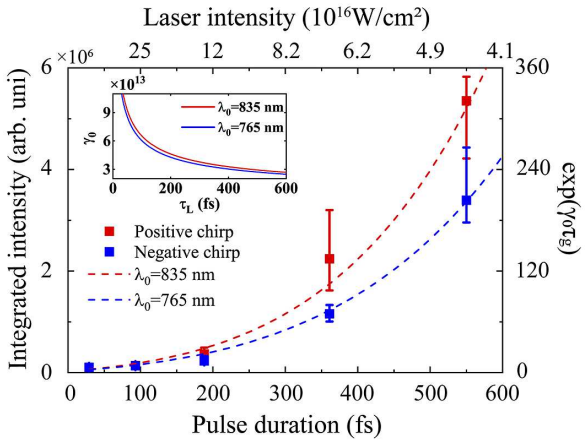

Figure 3. Integrated B-SRS spectral signal (840–1100 nm) versus pulse duration. The red solid squares are experimental results of positive ψ_2 and the blue solid squares correspond to negative ψ_2. The error bars are due to shot-to-shot fluctuations. The red dashed line presents the theoretical calculation of $e^{\gamma_0 t_g}$ with $\lambda_0 = 835$ nm, whereas the blue dashed line is that with $\lambda_0 = 765$ nm. The inset shows the calculated γ_0 with duration for $\lambda_0 = 835$ nm (red solid line) and $\lambda_0 = 765$ nm (blue solid line), respectively.

laser excitation, as a_0 is correlated with the laser wavelength. Based on the calculation, the total gain of B-SRS could be estimated by $G \approx \exp(\gamma_0 \tau_g)$ with growth time τ_g. The best fit of the measurements is obtained with $\tau_g = 0.75\tau_L$ and plotted in Figure 3. This confirmed the earlier studies that B-SRS is excited at the pulse front[6,21]. Interestingly, the crude estimation gives a similar growth time, which is shorter than the pulse duration. The growth of B-SRS with $|\psi_2|$ scales as $G \approx \exp(\gamma_0 \tau_g) \propto \exp(\sqrt{\tau_L})$.

3.2. *Influence of ψ_2 on S-SRS*

Figure 4 shows shadowgraphs of laser-produced plasma with different ψ_2. Filamentary structures were observed originating from the edge of the plasma channel due to the ionization of neutral atoms by side-scattered light[8,36,37]. The side-filamentation is more noticeable, with a higher $|\psi_2|$ occurring both in upward and downward directions. It is absent with $\psi_2 = 0$ fs^2(shown in Figure 1(c)). The filaments occupy a larger spatial region and have a longer length with a higher $|\psi_2|$, regardless of the sign of the chirp. Figure 5 plots the typical transverse profiles for $\psi_2 = 0$ and $\psi_2 = +500$ fs^2 at the different spatial positions. The density profiles are quasi-Gaussian distribution in the transverse direction, which gives rise to the observed beam divergence (marked by the white solid lines in Figures 1(c) and 4). One should notice that the transverse density profiles are almost the same for $\psi_2 = 0$ and $\psi_2 = +500$ fs^2, but the side-scattering was absent for $\psi_2 = 0$. This suggests the side-scattering could not be due to the beam divergence but rather the S-SRS.

The effect of ψ_2 on side-scattering can also be distinguished by comparing the length and number of side filaments. We found the difference in chirp is significant at a shorter pulse duration. For example, filamentation in the case of $\psi_2 = -500$ fs^2 (Figure 4(d)) is extremely weak compared to that with $\psi_2 = +500$ fs^2 (Figure 4(a)). However, for $\psi_2 = \pm 2000$ fs^2 (Figures 4(c) and 4(f)), the difference between the two cases becomes indistinguishable. The group velocity dispersion induced by laser chirp could contribute to the observation. The pulse compression (for positively chirped pulse) or stretch (for negatively chirped pulse) induced by the group velocity dispersion would reinforce or suppress the Raman process. Moreover, this phenomenon is strongly dependent on the chirp rate[26,27]. A higher chirp rate has a stronger impact. Considering the chirp rate is 3.8 times larger for $|\psi_2| = 500$ fs^2 than that for $|\psi_2| = 2000$ fs^2 (shown in Table 1), it is reasonable to observe a significant difference for the former cases.

In addition, with the increase of $|\psi_2|$, the lateral dimension of the plasma channel reduces as a result of reduced on-axis laser intensity due to pulse stretching. It is approximately 280 ±15 μm for $|\psi_2| = 500$ fs^2, approximately 200 ± 15 μm for $|\psi_2| = 1000$ fs^2 and approximately 140 ±10 μm for $|\psi_2| = 2000$ fs^2, respectively.

3.3. *Influence of ψ_2 on F-SRS*

Figures 6(a) and 6(b) show the transmitted spectra under positive ψ_2 and negative ψ_2, respectively. The spectra of transmitted light are mainly composed of the laser spectrum and a blue-shifted component due to the ionization-induced frequency shift[38,39]. The red-shifted spectrum is intriguingly absent. The influence of $|\psi_2|$ on F-SRS significantly differs from that on the backward and side-scattering. There is no pronounced enhancement on SRS with increasing $|\psi_2|$. For positive ψ_2, anti-Stokes sidebands emerge at $\psi_2 = +500$ fs^2 and become more obvious at $\psi_2 = +1000$ fs^2. A further increase in ψ_2 will not affect the intensity of anti-Stokes sidebands, while slightly modulating their intervals. Sidebands in the cases of $\psi_2 = +1000$ fs^2, $\psi_2 = +2000$ fs^2 and $\psi_2 = +3000$ fs^2 have comparable signal intensity, which may suggest saturation of F-SRS at longer pulse durations.

In addition, the laser chirp was found to have a significant impact on F-SRS. Sections 3.1 and 3.2 show similar features of B-SRS and S-SRS for both negative and positive chirps. For F-SRS, however, the transmitted optical spectrum depends significantly on the sign of the laser chirp. As shown in Figure 6(b), in all cases with a negative laser chirp, the spectra are similar to that with $\psi_2 = +500$ fs^2 in Figure 6(a). There is no distinguishable sign of anti-Stokes sidebands in F-SRS with a negative chirp, even though the pulse duration is stretched to 550 fs ($\psi_2 = -3000$ fs^2). This indicates that F-SRS is strongly suppressed with a negatively chirped pulse. This observation is consistent with theoretical estimation[26], where a laser with 12% bandwidth can eliminate Raman forward scattering.

https://doi.org/10.1017/hpl.2022.30 Published online by Cambridge University Press

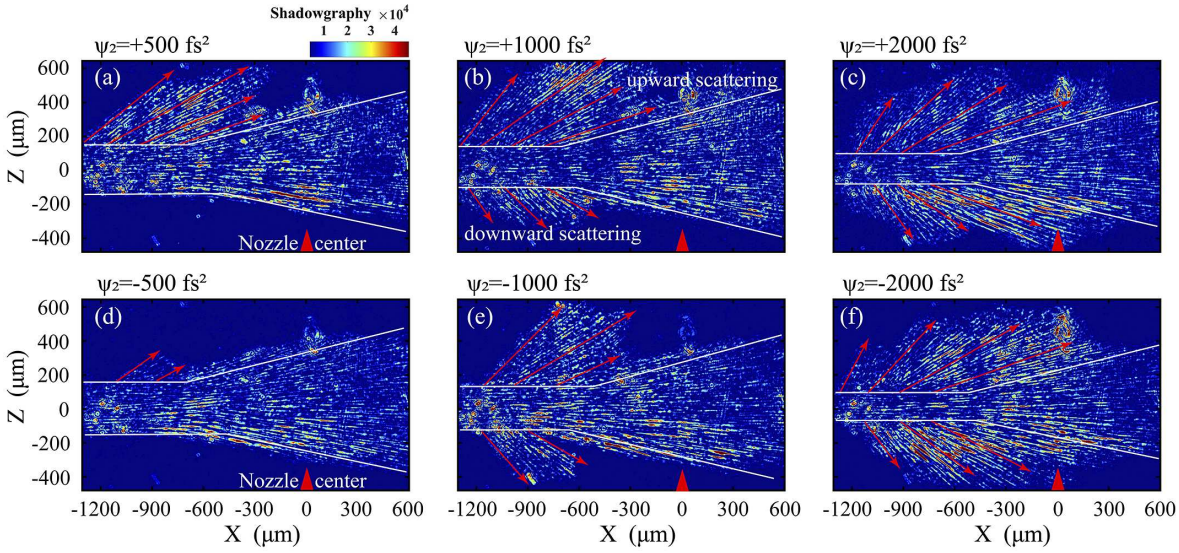

Figure 4. Shadowgraphs showing side filaments at different second-order dispersions ψ_2. (a) $\psi_2 = +500$ fs^2, (b) $\psi_2 = +1000$ fs^2, (c) $\psi_2 = +2000$ fs^2, (d) $\psi_2 = -500$ fs^2, (e) $\psi_2 = -1000$ fs^2 and (f) $\psi_2 = -2000$ fs^2. The red arrows denote the filament direction at different spatial position. The white lines show the edges of the plasma channel.

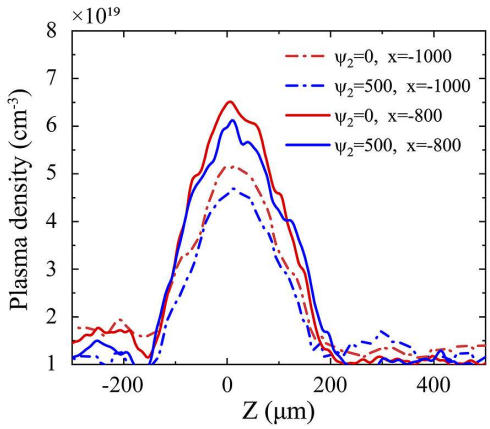

Figure 5. The transverse plasma density profile in the cases of $\psi_2 = 0$ and $\psi_2 = +500$ fs^2. The solid lines and the dash-dot lines represent the profiles obtained at $x = -800$ μm and $x = -1000$ μm, respectively.

3.4. Side-scattering angle dependence on ψ_2

As shown in Figure 4, there is a trend that the inclined angle of filaments relative to the laser axis gets smaller with the laser propagation (denoted by red arrows). In Figure 7, we plot the angles of both upward and downward filaments as a function of spatial position for different ψ_2. It shows that a relatively larger side-scattering angle is observed with a higher $|\psi_2|$. At $x = -1150$ μm, for instance, the angle increases from $31.0° \pm 4°$ for $|\psi_2| = 500$ fs^2 to $41.0° \pm 4°$ for $|\psi_2| = 2000$ fs^2. In Figures 7(b) and 7(c), the upward and downward side-scattering angles under positive and negative chirps are compared. The chirp effect is negligible, since the filament angles follow the same trends for both negative and positive ψ_2. Meanwhile, we note that the side-scatterings are asymmetric where the downward filaments have angles several degrees larger than that in the upward direction at the same spatial position. Similar observation has been reported by Matsuoka *et al.*[8]; however, the angular variation and underlying physics remain elusive.

To explain the spatially-dependent scattering angles, a model incorporating the growth of Raman scattering and the energy damping processes was used[2]. The energy damping rate of plasma waves is expressed as follows[2]:

$$\Gamma_p = \left(\frac{\pi}{8}\right)^{1/2} \frac{\omega_{pe}}{(k_p\lambda_D)^3} \exp\left[-\frac{1}{2}(k_p\lambda_D)^{-2} - \frac{3}{2}\right] + (\omega_{pe}/\omega_{epw})^2 \nu_{ei}, \quad (6)$$

where $\lambda_D = v_{th}/\omega_{pe}$ is the Debye length and ν_{ei} is the electron–ion collision frequency. The first term on the right-hand side in Equation (6) represents the Landau damping and the second term is the inverse bremsstrahlung absorption. The inverse bremsstrahlung absorption also causes an energy dissipation of the EM wave, giving $\Gamma_s = (\omega_{pe}/\omega_1)^2 \nu_{ei}$. Combining the two damping processes, the spatial growth rate of SRS is given as follows[2]:

$$\kappa = \left[\frac{\gamma_0^2}{v_{1x}v_{2x}} + \frac{1}{4}\left(\frac{\Gamma_s}{v_{1x}} - \frac{\Gamma_p}{v_{2x}}\right)^2\right]^{1/2} - \frac{1}{2}\left(\frac{\Gamma_s}{v_{1x}} + \frac{\Gamma_p}{v_{2x}}\right), \quad (7)$$

where v_{1x} and v_{2x} represent the group velocity of the scattered light and the plasma wave, respectively. They are expressed as follows:

$$v_{1x} = k_1 c^2 \cos\theta/\omega_1, \quad (8)$$

$$v_{2x} = 3(k_0 - k_1\cos\theta)\left(v_{th}^2/\omega_{pe}\right), \quad (9)$$

https://doi.org/10.1017/hpl.2022.30 Published online by Cambridge University Press

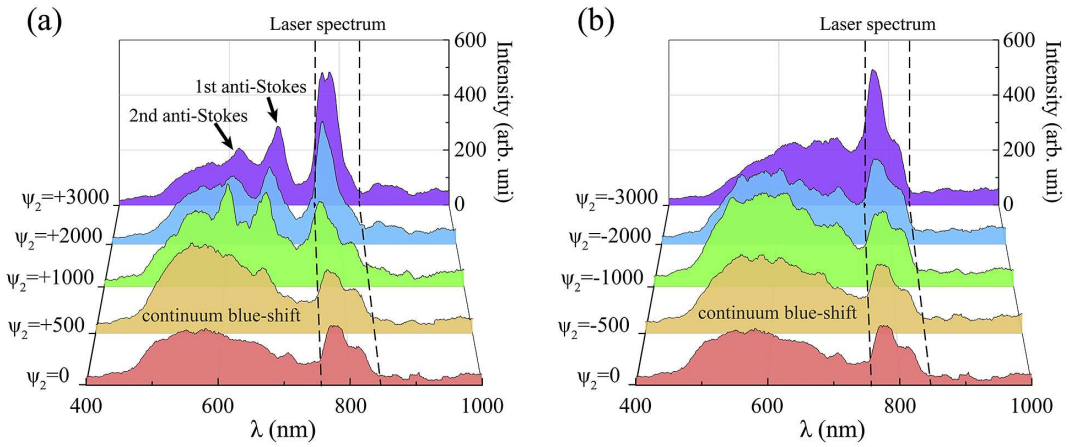

Figure 6. The spectra of transmitted light with (a) positive second-order dispersion and (b) negative second-order dispersion.

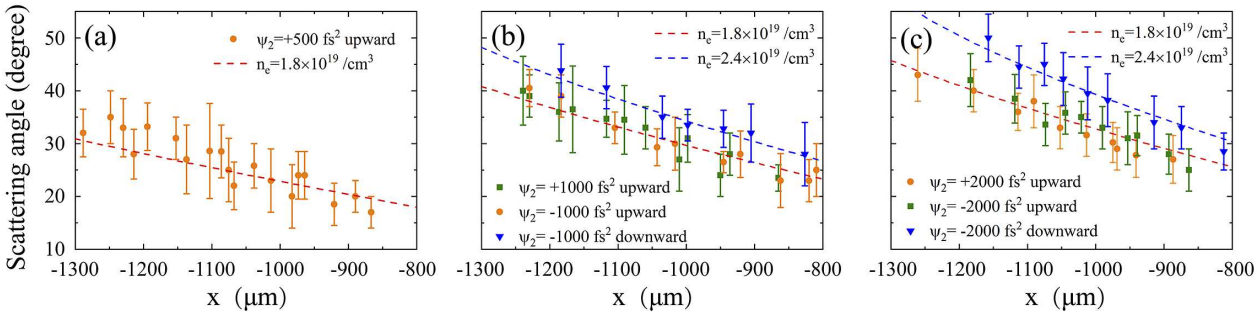

Figure 7. The side-scattering angle at different spatial positions with (a) $\psi_2 = +500$ fs^2, (b) $\psi_2 = \pm 1000$ fs^2 and (c) $\psi_2 = \pm 2000$ fs^2. Orange circles and green squares correspond to the measurements of the upward scattering angle with positive and negative ψ_2, respectively. Blue triangles are the measurements of the downward scattering angle with negative ψ_2. The orange (blue) dashed line is the calculation based on the maximum spatial growth rate with $n_e = 1.8 \times 10^{19}$ cm^{-3} ($n_e = 2.4 \times 10^{19}$ cm^{-3}).

where θ is the angle between the scattered light and the pump light. According to Equations (7)–(9), the spatial growth rate intrinsically depends on θ.

Since side filaments were found to originate from the plasma channel edge, the local plasma density n_e was used in calculating the growth rate κ. Deduced from the interferogram, n_e is $(1.8 \pm 0.3) \times 10^{19}$ cm^{-3} at the upper edge and $(2.4 \pm 0.3) \times 10^{19}$ cm^{-3} at the lower edge. Considering the laser focusing geometry, the laser intensity increases with the propagation. Plasma temperature T_e is estimated by the ATI ionization model described above.

Figure 8(a) shows the calculated plasma temperature distribution in the spatial position for different $|\psi_2|$. Here, T_e increases with the laser propagation and decreases with $|\psi_2|$. The calculated angular-dependent spatial growth rate κ is plotted in Figure 8(b). It shows that S-SRS has the largest growth rate along a cone angle near the forward direction[2,40]. The cone angle reduces with an increase in T_e or a decrease in n_e. We evaluated the influence of chirp on the spatial growth rate by changing the laser wavelength λ_0. The angle with maximum growth rate θ_m is weakly dependent on λ_0. For example, at $x = -1300$ μm, θ_m varies from 29.6° to 30.1° when λ_0 changes from 760 to 840 nm. The insensitivity of the scattering angle to the laser wavelength is consistent with our observations. Thus, the effect of chirp on the angle is trivial.

Since filaments should be most evident near θ_m, we plot θ_m as a function of spatial position (shown in Figures 5(a)–5(c)). The calculations successfully reproduce the measurements in all cases, which suggest that the reduced filament angle is mainly due to the increased T_e. During the laser propagation and focusing, the spot size decreases and T_e increases. Similarly, a larger θ_m is expected for a higher $|\psi_2|$, as the longer pulse duration will lower the temperature T_e. The measured asymmetric side-scattering in the upward and downward directions is evidently attributed to the n_e difference of plasma channel edges in the transverse direction.

4. Summary

In summary, we have reported a detailed study on the influence of the SOD, ψ_2, on SRS instability. The SRS is characterized in the backward, sideways, and forward directions.

https://doi.org/10.1017/hpl.2022.30 Published online by Cambridge University Press

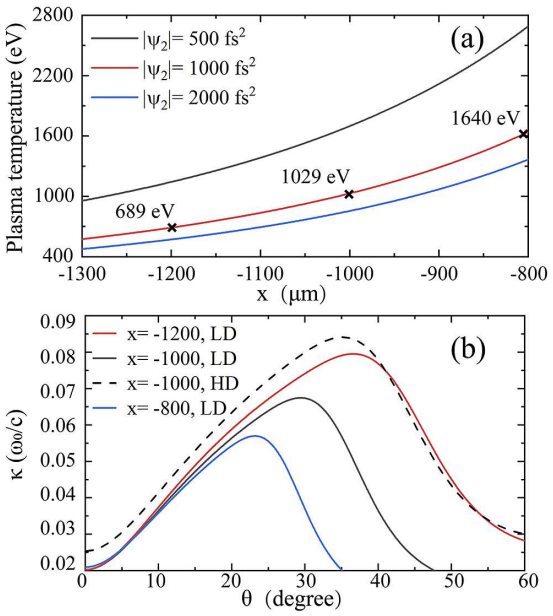

Figure 8. (a) The plasma temperature T_e for different $|\psi_2|$. (b) The typical angular distributions of the spatial growth rate that correspond to the black crosses in (a). LD is for $n_e = 1.8 \times 10^{19}$ cm^{-3}, and HD for $n_e = 2.4 \times 10^{19}$ cm^{-3}.

Evident excitation of SRS in all directions was observed when ψ_2 is introduced. B-SRS and S-SRS grow with $|\psi_2|$, and a stronger signal was measured with a positive ψ_2. However, there is a suppression of F-SRS when a negatively chirped pulse is used. Supported by a theoretical model, the spatially-dependent angle distribution of side-scattering is investigated. The side-scattering angle is defined by the plasma temperature and density and is insensitive to the laser chirp.

Acknowledgment

This work was supported by NSAF (No. U1930111) of China and the Strategic Priority Research Program of the Chinese Academy of Sciences (No. XDA25030200).

References

1. C. S. Liu, M. N. Rosenbluth, and R. B. White, Phys. Fluids **17**, 1211 (1974).
2. S. C. Wilks, W. L. Kruer, K. Estabrook, and A. B. Langdon, Phys. Fluids B **4**, 2794 (1992).
3. S. C. Wilks, W. L. Kruer, E. A. Williams, P. Amendt, and D. C. Eder, Phys. Plasmas **2**, 274 (1995).
4. T. M. Antonsen and P. Mora, Phys. Rev. Lett. **69**, 2204 (1992).
5. K. Krushelnick, A. Ting, H. R. Burris, A. Fisher, C. Manka, and E. Esarey, Phys. Rev. Lett. **75**, 3681 (1995).
6. K.-C. Tzeng, W. B. Mori, and C. D. Decker, Phys. Rev. Lett. **76**, 3332 (1996).
7. A. G. R. Thomas, S. P. D. Mangles, Z. Najmudin, M. C. Kaluza, C. D. Murphy, and K. Krushelnick, Phys. Rev. Lett. **98**, 054802 (2007).
8. T. Matsuoka, C. Mcguffey, P. G. Cummings, Y. Horovitz, F. Dollar, V. Chvykov, G. Kalintchenko, P. Rousseau, V. Yanovsky, S. S. Bulanov, A. G. R. Thomas, A. Maksimchuk, and K. Krushelnick, Phys. Rev. Lett. **105**, 034801 (2010).
9. E. Esarey, C. B. Schroeder, and W. P. Leemans, Rev. Mod. Phys. **81**, 1229 (2009).
10. T. Nakamura, S. V. Bulanov, T. Z. Esirkepov, and M. Kando, Phys. Rev. Lett. **105**, 135002 (2010).
11. M. H. Helle, D. F. Gordon, D. Kaganovich, Y. Chen, J. P. Palastro, and A. Ting, Phys. Rev. Lett. **117**, 165001 (2016).
12. O. Silva, M. Marti, J. R. Davies, R. A. Fonseca, C. Ren, F. S. Tsung, and W. B. Mori, Phys. Rev. Lett. **92**, 015002 (2004).
13. S. Corde, K. T. Phuoc, G. Lambert, R. Fitour, V. Malka, A. Rousse, A. Beck, and E. Lefebvre, Rev. Mod. Phys. **85**, 1 (2013).
14. G. B. Zhang, M. Chen, X. H. Yang, F. Liu, S. M. Weng, Y. Y. Ma, D. B. Zou, T. P. Yu, F. Q. Shao, and Z. M. Sheng, Opt. Express **28**, 29927 (2013).
15. A. Modena, Z. Najmudin, A. E. Dangor, C. E. Clayton, K. A. Marsh, C. Joshi, V. Malka, C. B. Darrow, C. Danson, D. Neely, and F. N. Walsh, Nature **377**, 606 (1995).
16. N. Hafz, M. S. Hur, G. H. Kim, C. Kim, I. S. Ko, and H. Suk, Phys. Rev. E **73**, 016405 (2006).
17. A. E. Hussein, J. Ludwig, K. Behm, Y. Horovitz, P.-E. Masson-Laborde, V. Chvykov, A. Maksimchuk, T. Matsuoka, C. McGuffey, V. Yanovsky, W. Rozmus, and K. Krushelnick, New J. Phys. **20**, 073039 (2018).
18. D. Kaganovich, B. Hafizi, J. P. Palastro, A. Ting, M. H. Helle, Y.-H. Chen, T. G. Jones, and D. F. Gordon, Phys. Plasmas **23**, 123104 (2016).
19. H. Jang, M. S. Hur, J. M. Lee, M. H. Cho, W. Namkung, and H. Suk, Appl. Phys. Lett. **93**, 071506 (2008).
20. W. P. Leemans, P. Catravas, E. Esarey, C. G. R. Geddes, C. Toth, R. Trines, C. B. Schroeder, B. A. Shadwick, J. van Tilborg, and J. Faure, Phys. Rev. Lett. **89**, 174802 (2002).
21. J. Faure, J.-R. Marquès, V. Malka, F. Amiranoff, Z. Najmudin, B. Walton, J.-P. Rousseau, S. Ranc, A. Solodov, and P. Mora, Phys. Rev. E **63**, 065401 (2001).
22. T.-W. Yau, C.-J. Hsu, H.-H. Chu, Y.-H. Chen, C.-H. Lee, J. Wang, and S.-Y. Chen, Phys. Plasmas **9**, 391 (2002).
23. B. S. Rao, A. Moorti, P. A. Naik, and P. D. Gupta, Phys. Rev. ST Accel. Beams **16**, 091301 (2013).
24. A. Permogorov, G. Cantono, D. Guenot, A. Persson, and C.-G. Wahlström, Sci. Rep. **12**, 3031 (2022).
25. H. T. Kim, V. B. Pathak, K. H. Pae, A. Lifschitz, F. Sylla, J. H. Shin, C. Hojbota, S. K. Lee, J. H. Sung, H. W. Lee, E. Guillaume, C. Thaury, K. Nakajima, J. Vieira, L. O. Silva, V. Malka, and C. H. Nam, Sci. Rep. **7**, 10203 (2017).
26. E. S. Dodd and D. Umstadter, Phys. Plasmas **8**, 3531 (2001).
27. V. B. Pathak, J. Vieira, R. A. Fonseca, and L. O. Silva, New J. Phys. **14**, 023057 (2012).
28. C. B. Schroeder, E. Esarey, B. A. Shadwick, and W. P. Leemans, Phys. Plasmas **10**, 285 (2003).
29. N. Pathak, A. Zhidkov, T. Hosokai, and R. Kodama, Phys. Plasmas **25**, 013119 (2018).
30. Y. Fang, T. P. Yu, X. L. Ge, S. Yang, W. Q. Wei, T. Yuan, F. Liu, M. Chen, J. Q. Liu, Y. T. Li, X. H. Yuan, Z. M. Sheng, and J. Zhang, Plasma. Phys. Control. F **58**, 45025 (2016).
31. P. Tournois, Opt. Commun. **140**, 245 (1997).
32. C. A. Coverdale, C. B. Darrow, C. D. Decker, W. B. Mori, K.-C. Tzeng, K. A. Marsh, C. E. Clayton, and C. Joshi, Phys. Rev. Lett. **74**, 4659 (1995).
33. P. B. Corkum, N. H. Burnett, and F. Brunel, Phys. Rev. Lett. **62**, 1259 (1989).
34. N. H. Burnett and P. B. Corkum, J. Opt. Soc. Am. B **6**, 1195 (1989).

https://doi.org/10.1017/hpl.2022.30 Published online by Cambridge University Press

35. M. V. Ammosov, N. B. Delone, and V. P. Krainov, Sov. Phys. JETP **64**, 1191 (1986).
36. F. Sylla, A. Flacco, S. Kahaly, M. Veltcheva, A. Lifschitz, G. Sanchez-Arriaga, E. Lefebvre, and V. Malka, Phys. Rev. Lett. **108**, 115003 (2012).
37. A. K. Arunachalam, M. B. Schwab, A. Sävert, and M. C. Kaluza, New J. Phys. **20**, 003027 (2018).
38. W. M. Wood, C. W. Siders, and M. C. Downer, Phys. Rev. Lett. **67**, 3523 (1991).
39. J. K. Koga, N. Naumova, M. Kando, L. N. Tsintsadze, K. Nakajima, S. V. Bulanov, H. Dewa, H. Kotaki, and T. Tajima, Phys. Plasmas **7**, 5223 (2000).
40. A. Higginson, S. Zhang, M. Bailly-Grandvaux, C. McGuffey, K. Bhutwala, B. J. Winjum, J. Strehlow, B. Edghill, M. Dozières, F. S. Tsung, R. Lee, S. Andrews, S. J. Spencer, N. Lemos, F. Albert, P. King, M. S. Wei, W. B. Mori, M. J.-E Manuel, and F. N. Beg, Phys. Rev. E. **103**, 033203 (2021).

https://doi.org/10.1017/hpl.2022.30 Published online by Cambridge University Press